Charge transport in InAs nanowire Josephson junctions

Simon Abay,[1,*] Daniel Persson,[1] Henrik Nilsson,[2] Fan Wu,[1] H.Q. Xu,[2,3] Mikael Fogelström,[1] Vitaly Shumeiko,[1] and Per Delsing[1,†]

[1] *Department of Microtechnology and Nanoscience (MC2), Chalmers University of Technology, SE-412 96 Göteborg, Sweden*
[2] *Division of Solid State Physics, Lund University, Box 118, S-221 00 Lund, Sweden*
[3] *Key Laboratory for the Physics and Chemistry of Nanodevices and Department of Electronics, Peking University, Beijing 100871, China*

(Dated: December 16, 2013)

We present an extensive experimental and theoretical study of the proximity effect in InAs nanowires connected to superconducting electrodes. We fabricated and investigated devices with suspended gate controlled nanowires and non-suspended nanowires, with a broad range of lengths and normal state resistances. We analyze the main features of the current-voltage characteristics: the Josephson current, excess current, and subgap current as functions of length, temperature, magnetic field and gate voltage, and compare them with theory. The Josephson critical current for a short length device, $L = 30\,\mathrm{nm}$, exhibits a record high magnitude of 800 nA at low temperature that comes close to the theoretically expected value. The critical current in all other devices is typically reduced compared to the theoretical values. The excess current is consistent with the normal resistance data and agrees well with the theory. The subgap current shows large number of structures, some of them are identified as subharmonic gap structures generated by Multiple Andreev Reflection. The other structures, detected in both suspended and non-suspended devices, have the form of voltage steps at voltages that are independent of either superconducting gap or length of the wire. By varying the gate voltage in suspended devices we are able to observe a cross over from typical tunneling transport at large negative gate voltage, with suppressed subgap current and negative excess current, to pronounced proximity junction behavior at large positive gate voltage, with enhanced Josephson current and subgap conductance as well as a large positive excess current.

I. INTRODUCTION

Semiconducting nanowires (NW) have been a focus of intensive research for their potential applications as building blocks in nano-scale devices.[1–4] The nano-scale dimension of the semiconducting nanowires, comparable to the electronic Fermi wave length, also makes them an attractive platform for studying the fundamental phenomena of quantum transport. By tuning the Fermi wavelength by means of electrostatic gates one gets access to such quantum phenomena as conductance quantization,[5,6] and quantum interference effects.[7]

Another research interest has been the proximity effect in nanowires induced by connecting them to superconducting electrodes (S).[8,9] In such devices, S-NW-S, the nanowire serves as a weak link through which a supercurrent can flow due to the presence of the phase difference between the superconducting condensates.[9–11]

Among a variety of nanowires tested in experiments, nanowires of InAs play a central role.[8,10] This is due to their material properties: high electron mobility, low effective mass, and pinning of the Fermi level in the conduction band that permits highly transparent galvanic S-NW contacts. Hybrid devices of InAs nanowires have demonstrated Andreev subgap conductance,[6,12,13] Josephson field effect,[9,10] and Cooper-pair beam splitting.[14] More recently, the nanowire hybrid devices attracted new attention following theoretical predictions of Majorana bound states in NW-S proximity structures.[15–17]

In spite of intensive research, no systematic investigation of the proximity effect in InAs nanowires has been reported, leaving open important questions about consistency of the observed transport phenomena and theoretical views of the proximity effect.

In this paper, we report on extensive experimental studies of current-voltage characteristics (IVC) of a large variety of hybrid devices made with InAs nanowires connected to aluminum electrodes. These Al-InAs NW-Al devices include suspended and non-suspended nanowires, nanowires with different lengths, and tested at different temperatures, magnetic fields, and gate voltages. We measured the main proximity effect characteristics: Josephson critical current, excess current, and subgap current features, and we make a quantitative comparison with relevant theoretical models.

Our main conclusion is that the most properties of the proximity effect can be qualitatively understood and quantitatively reasonably well fit on the basis of existing theory. In particular, the record high Josephson critical current of 800 nA, observed in the shortest studied nanowire (with 30 nm separation between superconducting electrodes) is close to the theoretical bound for ballistic point contacts.[18] In longer devices, the decay of the critical current with length is consistent with a cross over from ballistic to diffusive transport regime, followed by cross over from a short- to long-junction behavior.

In the gate controlled suspended devices we observe a cross over from a distinct S-normal metal-S (SNS) type behavior with large positive excess current and en-

hanced subgap conductance to tunneling S-insulator-S (SIS) type behaviour in accordance with gradual depletion of the conducting channels by the gate potential and increase of the wire resistance.

We also observe subgap current features associated with Multiple Andreev Reflection (MAR) transport. In addition to those MAR features we systematically observe subgap features, which are not associated with MAR but have some different origin. These features are not related to phonon-induced resonances,[19] and they do not seem to have an electromagnetic origin. They appear on the IVCs as voltage steps, strikingly similar to the voltage steps generated by phase slip centers in superconducting whiskers.[20,21]

The structure of the paper is as follows: After describing the device fabrication and experimental setup in Section II, we summarize the normal state conduction properties of the devices in Section III, which give the necessary input for choosing an appropriate theoretical model of the proximity effect described in Section IV. Then in the following sections we discuss the superconducting transport properties: excess current in Section V, critical current in Section VI, sub gap current, and variation of the current under the gate potential in Section VII. Section IX contains conclusive remarks.

II. EXPERIMENTAL DETAILS

A. Sample Fabrication

The devices we have investigated are of three types: nanowires placed directly on the substrate with either a) two superconducting contacts or b) multiple contacts, and c) suspended devices with local gates (Fig. 1). All devices are made on standard Si substrates capped by 400 nm thick SiO_2.

The nanowires are grown by chemical beam epitaxy.[22] In the growth process, metal-organic gaseous sources are thermally cracked to their components and the growth materials are directed as a beam towards an InAs substrate placed in the growth chamber. At the optimal temperature, the nanowire growth is catalyzed by Au aerosol particles that have been distributed on the substrate. The sizes of the Au-seeds determine the diameter of the nanowires. In this paper, the nanowires are taken from a single growth batch with an average diameter of 80 nm.

To fabricate the non-suspended devices, InAs nanowires are first transferred to a Si substrate and their relative positions with respect to predefined marks are determined with the help of scanning electron microscope (SEM) images. The extracted locations are then used to pattern superconducting Ti/Al (5/150 nm thick) contacts on top of the nanowires. Depending on the intended device length, *i.e.* distance between source and drain electrodes, the superconducting contacts are defined by either single-step or double-step electron beam (e-beam) lithography.[11] The shorter devices ($L < 100$ nm) are defined by the double-step e-beam lithography whereas the longer devices ($L \geq 100$ nm) are defined by the single-step e-beam lithography. A SEM image of a typical two terminal device ($L \approx 100$ nm defined by the single e-beam lithography) is shown in Fig. 1a. The inset image shows

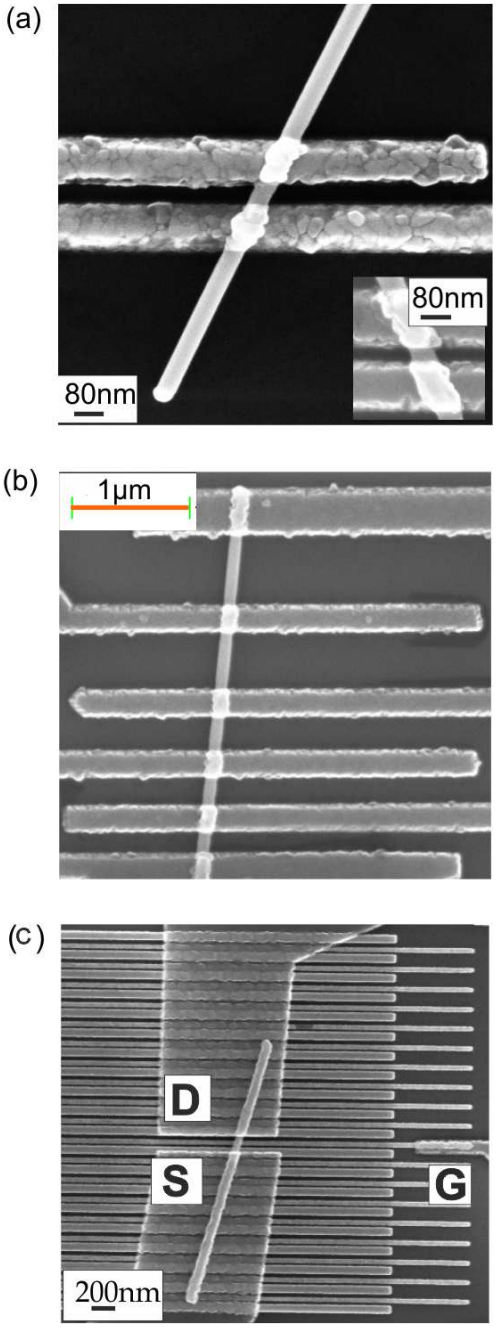

FIG. 1. SEM images of investigated devices. (a) Short length device of type A defined by a single-step electron-beam lithography (inset shows a short length device defined by a double-step e-beam lithography). (b) Device of type B has multiple contacts on a single nanowire separated by different lengths. (c) Three-terminal device with a suspended nanowire and a nearby local gate, the gate is 15 nm below the nanowire.

a short length device of $L \approx 60\,\mathrm{nm}$ defined by the double-step e-beam lithography.

To fabricate the suspended devices, a standard Si substrate is first patterned with interdigitated Ti/Au stripes.[23] InAs nanowires are then transferred to the already patterned Si substrate and some of the nanowires end up on top of the interdigitated metal stripes. The stripes are patterned in a two-step fabrication process in order to get a height difference of 15 nm between every two adjacent stripes. This allows the nanowires to rest on the thicker electrodes (65 nm thick) while being suspended above the substrate and the thinner electrodes (50 nm thick). With the help of SEM images, the positions of suitable nanowires are found and superconducting electrodes Ti/Al (5/150 nm thick) are defined on selected nanowires with e-beam lithography. A SEM image of a suspended device is shown in Fig. 1c.

To get good transparency of the metal-nanowire interfaces, an ammonium polysulfide solution (NH_4S_x) cleaning process[11,24] has been used prior to evaporation of the superconducting contacts. The samples are then characterized at room temperature and stored in a vacuum box before further measurements at low temperatures.

B. Experimental setup

Current-voltage characteristics of the devices are measured in a dilution refrigerator with a base temperature of 15 mK. The IVCs are recorded in either current or voltage bias configuration. In the current-bias mode, the current is determined by a high resistance bias resistor in series with the device. As we increase the current, the voltage across the device is simultaneously measured with a differential amplifier. In the voltage-bias mode, a voltage is directly applied across the device while the current is measured simultaneously by a transimpedance amplifier. To decrease noise coupling to the devices, the electrical lines in the measurement set up are well filtered and thermally anchored at different temperature stages of the refrigerator. The measurement setup is also designed to measure IVCs as a function of temperature and magnetic field.

C. Current-voltage characteristics

A typical IVC is shown in Fig. 2 for a device of length $L \approx 150\,\mathrm{nm}$ (sample B_{5a} in Table I). Above the critical temperature $T_c \approx 1.1\,\mathrm{K}$, the IVC (blue) exhibits Ohmic behavior with a normal-state resistance of $R_n = 1.07\,\mathrm{k\Omega}$. At temperatures well below T_c, the IVC (red) shows three distinct conductance regimes. i) For voltages $|V| > 2\Delta/e$, the IVC shows a linear behaviour with the same resistance as in the normal state, R_n. ii) For smaller voltages, $|V| < 2\Delta/e$, the resistance is approximately $R_n/2$ and exhibits subgap features. iii) At the zero voltage $V = 0$, the device switches to zero-resistance, exhibiting a Josephson current.

In the next sections we perform quantitative analysis of the IVC, based on a detailed characterization of the normal state current transport in the wire.

III. NORMAL STATE TRANSPORT

In order to characterize the normal-state properties of the junctions, dc-measurements have been performed on several devices with a broad range of lengths and resistances. Measurement results for representative devices are sumarized in Table I. The devices are divided into three groups: A, B, and C corresponding to the two-terminal, multi-terminal and suspended devices as shown in Fig. 1.

The normal state resistance as a function of length for devices B_5 and B_6 is plotted in Fig. 3. The resistance of each device increases linearly with length with approximately the same resistance per unit length, $R/L \approx 6\,\Omega/\mathrm{nm}$. Here, the resistance values are taken from the two-point measurements that also include interface resistance. From the length dependence of the resistance in Fig 3, we extract the contact resistance by extrapolating to zero length. For device B_5, we find that contact contribution is less than $180\,\Omega$, while for device B_6, it is approximately $1.2\,\mathrm{k\Omega}$.

Taking advantage of multiple contacts of the B type devices we perform two- and four-point measurements of the resistance, which allows us to determine the number of conducting channels and the channel average transparency. The two- and four-point resistance expres-

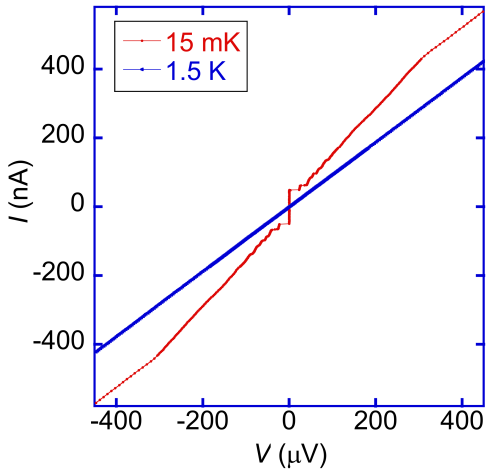

FIG. 2. Normal state IVC (blue line) and superconducting state IVC (red line) for a device of length $L \approx 150\,\mathrm{nm}$ (sample B_{5a}). The superconducting IVC shows normal state Ohmic behavior ($R_n = 1.07\,\mathrm{k\Omega}$) at $|V| > 2\Delta/e$, enhanced conductance and current features at subgap voltages $|V| \leq 2\Delta/e$, and the Josephson current.

Device		L(nm)	R_n(kΩ)	I_c(nA)	eI_cR_n/Δ	$eI_{exc}R_n/\Delta$
A	1	30	0.16	800	1.02	1.52
	2	90	0.55	95	0.40	0.87
	3	100	0.56	54	0.23	0.75
	4	220	1.04	30	0.24	0.76
B	5a	150	1.07	50	0.41	1.20
	5b	170	1.28	40	0.39	1.28
	5c	180	1.34	36	0.37	1.31
	5d	190	1.37	35	0.36	1.11
	6a	110	1.84	23	0.32	1.21
	6b	200	2.40	12	0.21	0.81
	6c	250	2.72	9	0.20	0.77
	6d	500	4.21	3	0.10	0.71
	6e	600	4.82	1	0.04	0.64
C	7	200	2.23	15	0.24	1.30
	8	150	3.3	13	0.34	1.17
	9	130	2.19	28	0.47	1.02
	10	300	3.80	6	0.17	1.23
	11	150	5.01	2.6	0.10	0.78
	12	200	3.6	7.5	0.21	1.11

TABLE I. Measurement values for devices of different types. Type A devices are nanowires with two superconducting contacts. Type B devices are defined on a single nanowire with multiple contacts. Adjacent junctions in the B-type devices are marked with alphabetic letters. Type C devices are suspended devices with local gates. The nanowires are taken from the same growth batch of approximately 80 nm in diameter.

sions can be written for perfect interfaces as $R_{2p} = R_q/(NT_t)$ and $R_{4p} = R_q(1-T_t)/(NT_t)$, respectively,[25] where $R_q = h/2e^2 = 12.9\,\mathrm{k\Omega}$ is the quantum of resistance, N is the number of channels and T_t is the average transparency of the channels. Taking two- and four-point resistance measurements on the same section, we find that our nanowires have a spread in the number of channels ranging between 50 and 100 channels. For instance, for junction B_{5c}, we measured $R_{2p} = 1.34\,k\Omega$, and $R_{4p} = 1.18\,k\Omega$, giving the number of channels

$$N = \frac{R_q}{R_{2p} - R_{4p}} \approx 80. \qquad (1)$$

This is consistent with the contact resistance found for device B_5, and implies perfect S-NW interfaces with transparency close to unity. For the same junction we can then extract the average transparency $T_t = 0.12$ for the channels.

Assuming only a surface layer of nanowire to be conducting, in analogy with the 2DEG conductivity in planar InAs devices, such a large amount of conducting channels would give unrealistically small value for the Fermi wavelength. On the other hand, assuming the whole bulk of the wire to be conducting we find the electronic Fermi wave length λ_F to depend logarithmically

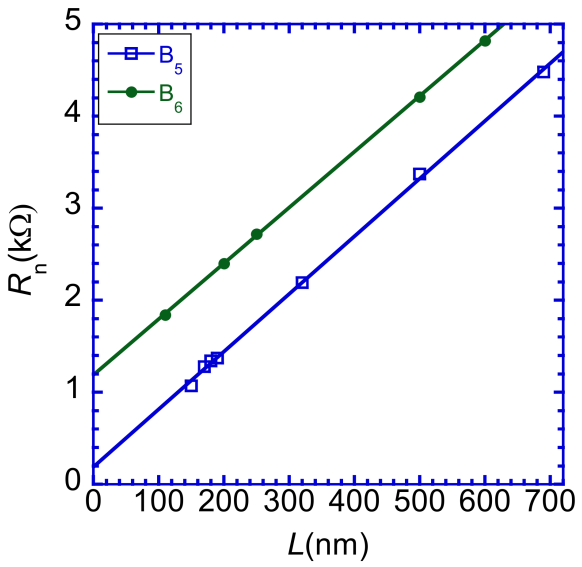

FIG. 3. Normal state differential resistance as a function of length for devices B_5 (blue line) and B_6 (green line). The two devices show approximately the same resistance per unit length 6 Ω/nm. Extrapolating to zero length gives the full contact resistance, less than 180 Ω for B_5, and 1.2 $k\Omega$ for B_6.

on the number of channels, as

$$\lambda_F(N) = \frac{2\pi r_w}{\alpha_{l,n}} \approx A - B\ln(N). \qquad (2)$$

This result is arrived at by solving the Schrödinger equation in a cylinder of radius r_w and counting the number of modes (channels) that cross the Fermi level. In Eq. (2) $\alpha_{l,n}$ is the n-th zero of the J_l-th Bessel function, l labels the last mode that contributes to transport. The coefficients A and B in Eq. (2) are functions of the nanowire radius; for $r_w = 40\,\mathrm{nm}$, $A = 42.4\,\mathrm{nm}$ and $B = 7.63\,\mathrm{nm}$, and varying the radius by ±10% will change both coefficients approximately by ±2%. We can bracket the Fermi wave length between, $\lambda_F \approx 17\,\mathrm{nm}$ (100 channels) and $\lambda_F \approx 22\,\mathrm{nm}$ (50 channels) for $r_w = 40\,\mathrm{nm}$. Our values are consistent with the ones reported for planar InAs 2DEG ($\lambda_F \approx 18\,\mathrm{nm}$),[26] and for InAs nanowires ($22\,\mathrm{nm} \lesssim \lambda_F \lesssim 33\,\mathrm{nm}$).[7] In the further discussions we adopt the values, $\lambda_F = 22\,\mathrm{nm}$, and N =55 for all the junctions.

Furthermore we use the measured resistance per unit length, $R/L = 6\,\Omega/\mathrm{nm}$, together with the expression for the Drude conductivity, $\sigma = ne^2\tau/m$, to evaluate a mean free path for the nanowires of $\ell_e = 46\,\mathrm{nm}$. The corresponding Fermi velocity $v_F = \hbar k_F/m^* \approx 1.3\times10^6\,\mathrm{m/s}$ is evaluated by using an electronic effective mass $m^* = 0.026m_e$ of bulk InAs, where m_e is the free electron mass. The effective mass of electrons m^* for planar InAs 2DEG has been estimated to be in a range from 0.024 to 0.04 × m_e.[26,27] The normal state properties of the nanowires are summarized in Table II.

Fermi wavelength λ_F	(nm)	22
Fermi wavevector k_F	(m^{-1})	$2.9 \cdot 10^8$
Fermi velocity v_F	(m/s)	$1.3 \cdot 10^6$
Mean free path ℓ_e	(nm)	46
# conducting channels		55
Superconducting gap Δ	(μeV)	160
Clean coherence length ξ_0	(nm)	1300
Diffusive coherence length ξ_D	(nm)	245
Diffusion constant $D_{\rm diff}$	(cm^2/s)	200
$e\Delta/\pi\hbar$	(nA)	12.6

TABLE II. Summary of the extracted parameters for the nanowires.

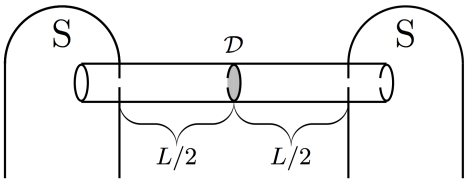

FIG. 4. A schematic picture of the theoretical model for the nanowire junctions: Superconducting electrodes (S) are connected by a disordered nanowire of length L, which also contains crystalline defects; the latter are modeled with a lumped scatterer situating in the middle of the wire and having effective transparency $\mathcal{D}$; the applied voltage is assumed to mostly drop at the scatterer.

IV. THEORETICAL MODEL

The major difficulty for theoretical interpretation of the experimental data is the very large spread of the wire lengths. Indeed, the shortest wire (30 nm) is in the ballistic point contact regime ($L < \ell_e, \xi_0$, with $\xi_0 = \hbar v_f/2\pi k_B T_c$), while the longest wire is in the diffusive long junction regime ($L > \ell_e, \xi_D$, with $\xi_D = \sqrt{\ell_e \xi_0}$). The majority of the junctions are in the intermediate cross over region. Furthermore, all the tested junctions exhibit the Josephson effect. This implies that the current transport is fully coherent and requires theoretical modeling within the framework of the coherent MAR theory.[28–31] To overcome this difficulty, we adopt a simple and tractable model, with which we can bridge between the ballistic and diffusive transport regimes, and describe the cross over to the long junction behavior.[32] The model setup is shown in Fig. 4. We assume that the two superconducting leads are connected to the nanowire by highly transmissive contacts, which are treated as fully transparent. The nanowire is disordered due to elastic scattering by impurities and crystal imperfections. This is treated in the Born approximation and the mean free path estimated from the experiments $\ell_e = 46\,$nm infers a scattering rate $\Gamma = v_F/\ell_e \approx 2.8 \cdot 10^{13} s^{-1}$. Strong defects are included and treated as a single interface having the same effective transparency $\mathcal{D}$ for all conducting channel. This defect is assumed to be in the centre of the nanowire, and the applied voltage to drop at the defect.

Using the quasi-classical Green's function methods described in Refs. 33 and 34, we calculate the IVC as function of device length and transparency by solving the coherent MAR problem. The current is calculated at the scatterer[33] and expressed through the boundary values, $\hat{g}_{R/L} = \hat{g}(\hat{\vec{p}}_F, x = \pm 0; \omega)$, of the quasi-classical Green's function for a given channel,

$$\hat{g}(\hat{\vec{p}}_F, x; \omega) = \begin{pmatrix} g(\hat{\vec{p}}_F, x; \omega) & f(\hat{\vec{p}}_F, x; \omega) \\ \tilde{f}(\hat{\vec{p}}_F, x; \omega) & -g(\hat{\vec{p}}_F, x; \omega) \end{pmatrix}, \ \hat{g}^2 = -\pi^2. \tag{3}$$

The Green's function is computed by solving the Eilenberger equation in the right and left parts of the nanowire,

$$i\hbar \vec{v}_F \cdot \vec{\partial}_x \hat{g}(\hat{\vec{p}}_F, x; \omega) + [\varepsilon(x; \omega)\hat{\tau}_3 - \hat{\Delta}_{\rm imp}(x; \omega), \hat{g}(\hat{\vec{p}}_F, x; \omega)] = 0, \tag{4}$$

complemented with the Zaitsev boundary conditions at the scatterer and NW-S interfaces.[33–35] $\hat{\tau}_3$ is the third Pauli matrix in Nambu space. In Eq. (4) we introduce the impurity scattering via the impurity self-energies

$$\varepsilon(x; \omega) = \hbar\omega - \hbar\Gamma \langle g(\hat{\vec{p}}_F, x; \omega) \rangle_{p_F}, \tag{5}$$

$$\hat{\Delta}_{\rm imp}(x; \omega) = \hbar\Gamma \langle \hat{f}(\hat{\vec{p}}_F, x; \omega) \rangle_{p_F}, \tag{6}$$

$\langle \cdots \rangle_{p_F}$ is average over directions ($\pm\hat{\vec{p}}_F$). The matrix $\hat{f}$ is the anomalous (off-diagonal) part of the Green's function $\hat{g}$. The components $(f, \tilde{f})$ of $\hat{f}$ describe the pairing correlations leaking in to the nanowire and two are related by symmetry as $\tilde{f}(\hat{\vec{p}}_F, x; \omega) = -f^*(-\hat{\vec{p}}_F, x; -\omega^*)$.

V. EXCESS CURRENT

We start with a discussion of the excess current at large voltage, which is a robust feature of the proximity IVC. The excess current, $I_{\rm exc}$, is extracted from the current-voltage characteristics at large voltage bias using the asymptotic form $I(V > 2\Delta/e) \approx V/R_N + I_{\rm exc} + \mathcal{O}(\Delta/eV)$. The excess current contains contributions both from the single-particle and from the two-particle Andreev currents, and it linearly scales with the energy gap $\Delta(T)$ (see *e.g.* Ref. 36). In Fig. 5a, the excess current is obtained for the device B_{5a} by extrapolating a linear fit of the IVC measured at $V > 2\Delta/e$ (blue dashed line) giving $I_{exc} = 150\,$nA. To verify that the measured excess current derives from Andreev scattering processes the experimentally extracted excess current is plotted as a function of temperature in Fig. 5b. As can be seen the amplitude of the excess current follows the temperature dependence of the superconducting gap $\Delta(T)$.

The excess current also depends on the transparency and the length of the nanowire device. In Fig. 6 we present the computed excess current as function of device

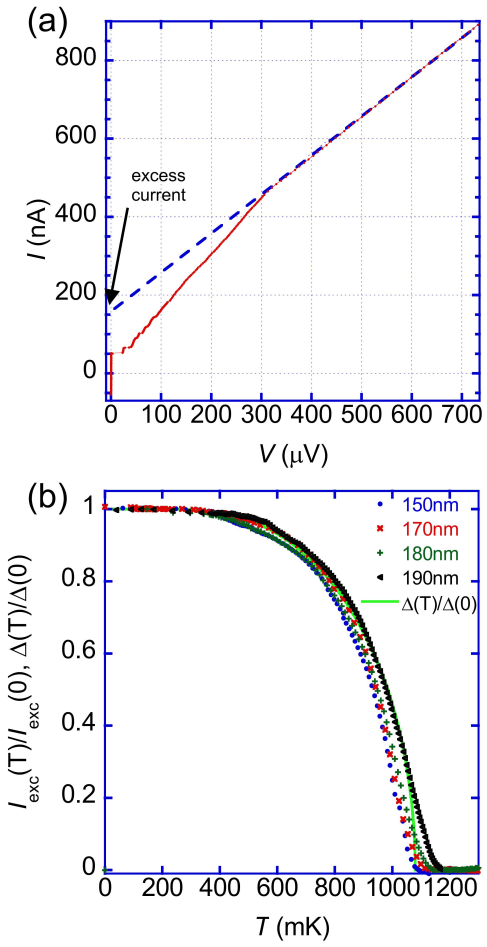

FIG. 5. a) Current-voltage characteristics of the device B_{5a} with length $L = 150\,\text{nm}$ and normal state resistance $R_n = 1.07\,\text{k}\Omega$. The excess current is extracted by extrapolating the IVC from high voltage to zero voltage. b) Excess currents as a function of temperature are shown for device B_5 (L= 150 nm, 170 nm, 180 nm, and 190 nm). The excess currents follow the superconducting energy gap $\Delta(T)$ (light green).

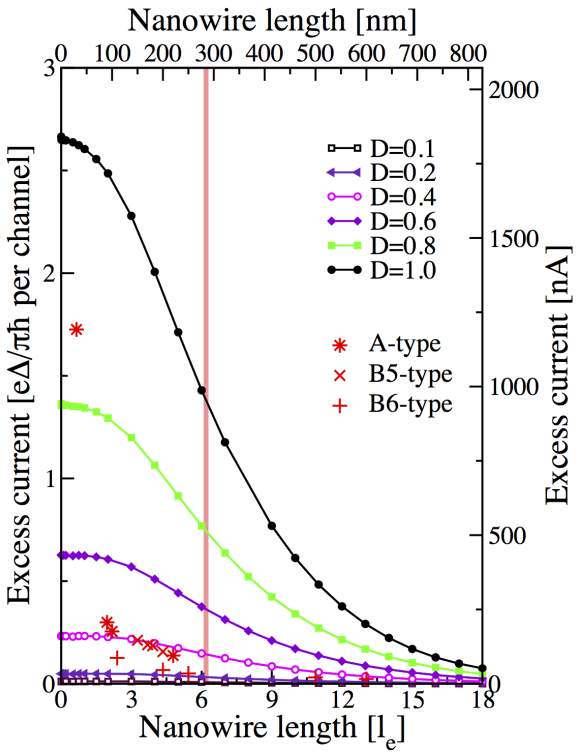

FIG. 6. The computed excess current as a function of length and effective transparency of the device. The units of the excess current are given on the left axis for the single channel and to the right in nA assuming that all channel have the same average transparency. The length of the device is given both in units of the mean free path (bottom x-axis) and in nm (top x-axis). The vertical line indicates the length $L = \sqrt{\hbar D_{\text{diff}}/\Delta} \approx 1.1\xi_D$, where the Thouless energy, $E_{\text{Th}} = \hbar D_{\text{diff}}/L^2$, equals the superconducting gap; this length separates the short-junction limit ($E_{\text{Th}} \gg \Delta$) from the long-junction limit ($E_{\text{Th}} \ll \Delta$). The stars and crosses are the experimental data from Table I; as can be seen the most devices are in the intermediate limit where $E_{\text{Th}} \approx \Delta$.

length together with I_{exc} extracted from the measurements. The maximum values of the theoretical curves correspond to the point contact limit ($L = 0$), and they are in a good agreement with analytical results[36], $I_{\text{exc}} = (8/3\pi)(e\Delta/\hbar)$ per channel for $\mathcal{D} = 1$, and $I_{\text{exc}} \approx \mathcal{D}^2(e\Delta/\hbar)$ for $\mathcal{D} \ll 1$. When the wire length is increased the excess current decreases. This was also found, experimentally and theoretically, in ballistic 2DEG InAs,[26], and computed for fully diffusive junctions.[37,38] In our case, the experimental values fall on curves with a typical effective transparency between 0.2 and 0.4 being only weakly device dependent between batches of nano wires. These values compare favorably with $T_t = 0.12$ extracted from the 2-point and 4-point measurements in the normal state.

One device, A_1 (L=30 nm), however, stands out showing a high transparency of $\mathcal{D} \approx 0.87$. For this junction, highly transmissive ballistic point contact, one should anticipate the largest critical current.

VI. JOSEPHSON CURRENT

Next, we discuss the Josephson critical current as a function of length, temperature, and magnetic field. The critical current values, I_c, are extracted from the experimentally obtained IVC at the base temperature of 15 mK and shown in Table I. The critical currents exhibit a range of values depending on the resistance and length of the devices, from a few nA to 800 nA. Similarly, the characteristic voltage, the I_cR_n-product, also exhibits a range of values, from 20 μV to 130 μV.

Theoretically, the Josephson current-phase relation is computed using boundary values of the Green's function,

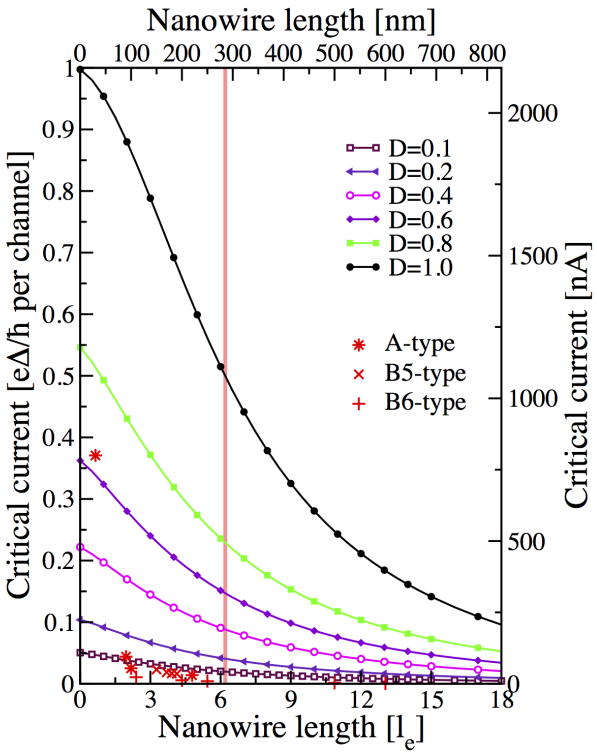

FIG. 7. The computed critical current as a function of length and effective transparency of the device. The units of the critical current are given on the left axis for the single channel and to the right in nA assuming that all channel have the same average transparency. The length of the device is given both in units of the mean free path (bottom x-axis) and in nm (top x-axis). The single markers are the experimental values reported in Table I.

$\hat{g}(\hat{\vec{p}}_F, x; \omega)$, in Eqs. (3) and (4), the expression reads,[35]

$$I_s(\phi) = \frac{8\pi e T \mathcal{D}}{h} \sum_{\omega_n > 0} \left\langle \frac{f_R f_L \sin\phi}{2 - \mathcal{D}(g_R g_L - f_R f_L \cos\phi + 1)} \right\rangle_{p_F} . \quad (7)$$

The sum is over all Matsubara frequencies, $\omega_n = \pi k_B T(2n+1)$, T is the temperature, ϕ the phase difference over the junction. The critical current is obtained by maximizing the supercurrent.

The critical current for the devices presented in Table I, together with a theoretical fit, as a function of length, is plotted in Fig. 7. The shortest junction exhibits the largest critical current, as expected, with the theoretical fit of the transparency, $\mathcal{D} \approx 0.65$. This is very close (75%) to the theoretical limit defined by the transparency extracted from the analysis of the excess current.

The other junctions fall in the transparency region $0.05 < \mathcal{D} < 0.1$, which is somewhat smaller compared to the transparency extracted from the excess current.

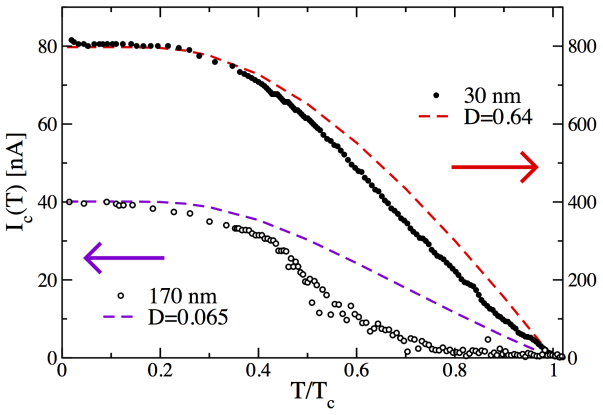

FIG. 8. Critical current as a function of temperature for two devices of length $L = 30\,\text{nm}$ and $L = 170\,\text{nm}$. Note the different scales for the current magnitude. Theoretical fits for both devices are shown. The transparency chosen to fit the data is taken from the low-temperature values for I_c in Fig. 7.

This implies that the critical current is reduced (approximately by a factor of 4) compared to the theoretical values. Similar or even larger reduction of Josephson current is commonly observed in nanowires, and it is also common in 2DEG InAs Josephson junctions[26]. Such an effect is not well understood, perhaps it could be related to some depairing mechanism, for example due to magnetic scattering. Part of the reduction could be explained by premature switching from the zero-voltage state due to fluctuations. The measurement of the IVC takes approximately 1 minute. The sample thus spends approximately a few seconds close to I_c.

The critical current is also investigated as a function of temperature for several devices. The critical currents for the shortest length device A_1 ($L \approx 30\,\text{nm}$ and $R_n = 0.16\,\text{k}\Omega$), and for the somewhat longer device B_{5b}, ($L \approx 170\,\text{nm}$ and $R_n = 1.15\,\text{k}\Omega$), are shown in Fig. 8. At the base temperature $T = 15\,\text{mK}$, the devices have critical currents of $I_c = 800\,\text{nA}$ and $40\,\text{nA}$, respectively. The data for the shortest device agree well with theory in a broad range of temperatures. The longer device exhibits a concave shaped decay at higher temperatures and deviates from the theoretical fit. Qualitatively similar shape of $I_c(T)$ has been theoretically found for diffusive junctions with highly resistive interfaces (SINIS),[39] and explained with enhancement of electron-hole dephasing in the proximity region due to large dwell time. Such an effect is similar to the effect of increasing length of the junction (*cf.* Ref. 38). Given such a similarity we may conclude that although device B_5 has transparent S-NW interfaces, the model[39] might better capture the effect of the junction length. On the other hand, critical current suppression at elevated temperature might result from premature switching of the device to the dissipative

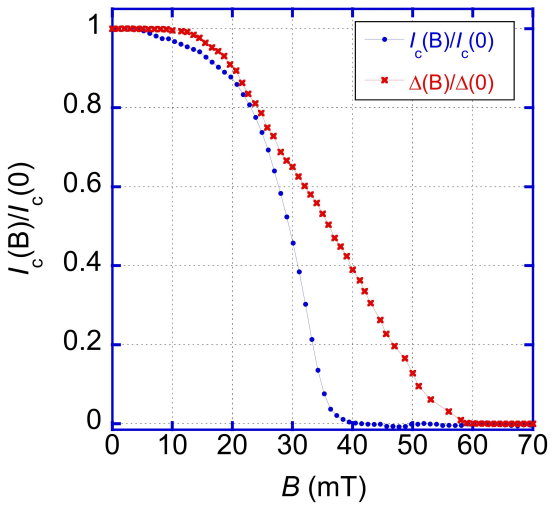

FIG. 9. Normalized critical current as a function of magnetic field for device A_1 ($L = 30\,\mathrm{nm}$) along with the measured superconducting energy gap $\Delta(B)$.

branch due to thermal fluctuations or other noise sources.

At the base temperature of 15 mK, we also have obtained IVCs as a function of magnetic field. The magnetic field is applied perpendicular to the superconducting leads. The normalized critical current and the superconducting energy gap as a function magnetic field are plotted in Fig. 9 for device A_1 with $L = 30\,\mathrm{nm}$. The superconducting gap $\Delta(B)$ is extracted from the voltage position of the gap feature, $V = 2\Delta/e$. The critical current decreases and is totally suppressed at a magnetic field of $B \approx 40\,\mathrm{mT}$. No Fraunhofer oscillations are observed in any of the devices, consistent with a suppression of superconducting energy gap in the leads. On the other hand, the gap feature on the IVC persists to higher magnetic field and disappears at the critical value $B_c \approx 60\,\mathrm{mT}$. The nature of this discrepancy is not clear, perhaps it results from the same depairing mechanism that suppresses the overall critical current, or fluctuation mechanism that suppresses the Josephson current at high temperatures.

VII. SUBGAP CURRENT

Now we proceed with discussion of the IVC in the subgap region, $V < 2\Delta/e$, as function of temperature and magnetic field, and for different nanowire lengths. A typical plot of the differential resistance as a function of voltage is presented in Fig. 10a. The resistance drops from $R_n = 1.15\,\mathrm{k\Omega}$ at $V \gg 2\Delta$ to $R_{SG} \approx 0.7\,\mathrm{k\Omega}$ at $V \approx 260\,\mu\mathrm{V}$, which corresponds to the gap value, $2\Delta/e$. Such a drop of resistance in the subgap region is a characteristic of Andreev transport in transmissive SNS junctions.[40] Furthermore, the differential resistance shows a second feature at approximately half the gap voltage, $V \approx 130\,\mu\mathrm{V} = 2\Delta/2e$ (shown by arrow in Fig. 10a).

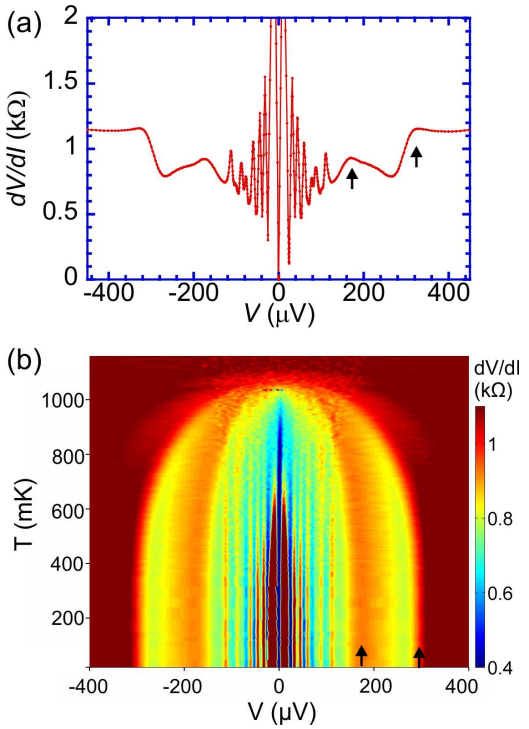

FIG. 10. (a) Differential resistance dV/dI as function of voltage for device B_{5b} ($L = 170\,\mathrm{nm}$ and $R_n = 1.15\,\mathrm{k\Omega}$). The resistance substantially decreased at $V \approx 2\Delta/e$ and exhibits symmetric resistance peaks/dips. (b) An image plot of differential resistance dV/dI as a function of voltage and temperature. As the temperature is increased, the first two peaks, marked by two arrows, smoothly move towards lower voltages consistent with the decrease of the superconducting energy gap $\Delta(T)$. However, the voltage positions of the other peaks are independent of temperature.

Positions of both these features scale with the temperature dependence of the superconducting gap $\Delta(T)$, as shown on Fig. 10b. This unambiguously indicates the MAR transport mechanism. Similar features associated with MAR are observed in all measured devices, in some devices we also observed a third MAR feature at $2\Delta/3e$.

We have also measured the dependence of positions of the resistance features as a function of magnetic field. The differential resistance of device A_4 as function of magnetic field is shown in Fig. 11. In this device, the three MAR features are present (marked by arrows), which move smoothly towards lower voltages following the magnetic field dependence of the gap $\Delta(B)$.

Besides the MAR features, the IVC of all the measured devices exhibit a number of structures at lower voltages, whose positions are independent of both temperature and magnetic field, see Fig. 10 and Fig. 11. These structures are therefore not associated with MAR. However, they are related to the superconducting state in the electrodes

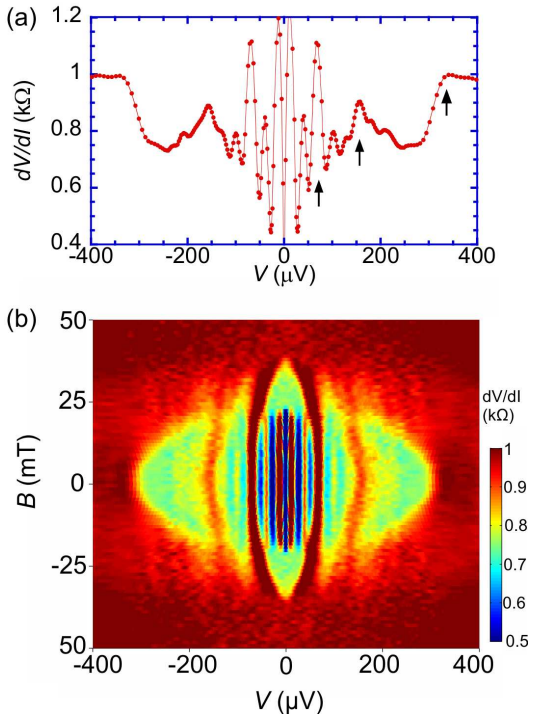

FIG. 11. (a) Differential resistance dV/dI as a function of voltage for device A_4. There are three MAR features indicated with arrows. (b) An image plot of differential resistance dV/dI as a function of voltage and magnetic field. As the magnetic field is increased, the MAR resistance peaks smoothly move towards lower voltages consistent with the decrease of the superconducting energy gap $\Delta(B)$. However, the voltage positions of the other peaks are independent of magnetic field.

since they do not persist above the critical temperature and critical magnetic field and even disappear somewhat earlier.

The origin of these structures is not clear. In Ref. 19 similar structures were reported for suspended NW devices and attributed to resonances resulting from coupling of the ac Josephson current to mechanical vibrations in the wire. The fact that we observe such structures not only in suspended but also in non-suspended wires rules out this explanation. Furthermore, the phonon resonances would appear at voltages corresponding to the phonon eigen-frequencies, i.e. depend on the wire length ($\propto 1/L$). We systematically measured the length dependence of the low-voltage, temperature independent structures, the results are presented in Fig. 12. The positions of the structures do not depend on the wire lengths neither for suspended nor non-suspended devices. The positions are given by the integer multiples of the same voltage, $V \approx 24\,\mu$V.

The fact that the positions of the temperature-independent structures are the same in different junctions makes it unlikely that they are related to external electromagnetic resonances, but rather result from some general intrinsic mechanism. To get a better insight in

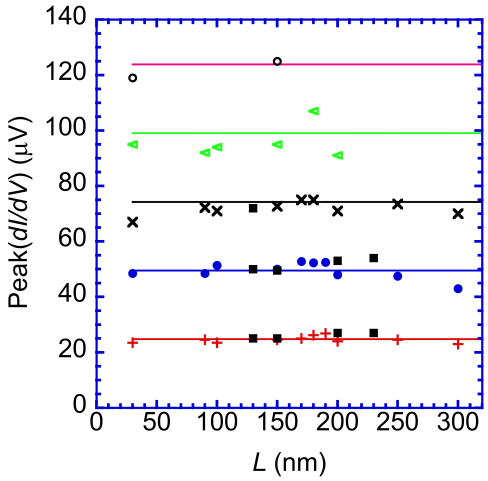

FIG. 12. Voltage positions of the temperature independent differential conductance peaks as function of length for devices of type A, B and C. Horizontal lines indicate the multiples of the voltage $V \approx 24\mu$V.

the origin of the temperature independent subgap structures we analyzed the shape of the IVC, see Fig. 13. In all investigated junctions the IVC have a staircase shape and consist of a number of successive voltage steps. Between the steps, the current continuously grows with the differential resistance increasing after every step. Such a behavior may be explained by successive emergence of normally conducting domains in the wire as soon as the current exceeds the critical value. This picture closely resembles the resistive states in superconducting whiskers containing phase slip centers (PSC).[20,21] Although one cannot in a straightforward way extend the PSC scenario in truly superconducting whiskers[41] to the proximity induced superconductivity in nanowires, one cannot exclude the possibility of formation of some kind of spatially inhomogeneous resistive state in the proximity region.

VIII. GATE DEPENDENCE

In this section, we investigate the gate dependence of the IVC in the superconducting state of suspended devices of type C shown in Fig. 1 and in Table I. The gate voltage controls the conductance by locally changing the carrier concentration and thereby creating a potential barrier in the conduction paths. In our devices, the gate is strongly capacitively coupled to nanowire, and the variation of the gate voltage has a profound effect on the conductance at low temperatures. As a result, the critical current and the IVC change significantly with the gate.

The dependence of the Josephson critical current on the gate voltage is shown in Fig. 14a for the suspended device C_{11} ($L \approx 150\,$nm). The change of the critical current (blue) varies in tact with the change of the differential conductance (red). Owing to the n-type nature of

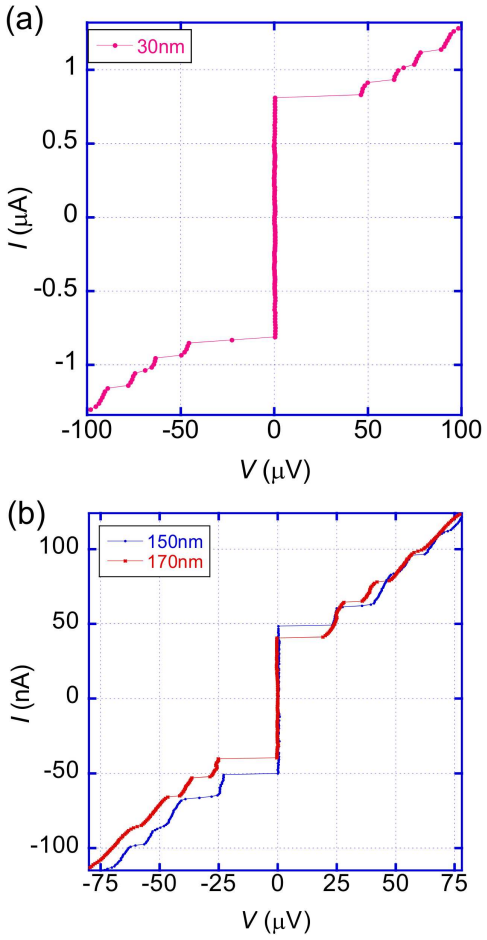

FIG. 13. Current voltage characteristics at low voltages for device A_1 (length $L = 30\,\mathrm{nm}$ and normal state resistance $R_n = 0.16\,\mathrm{k\Omega}$). The device shows successive voltage jumps with the resistance continuously increasing just after each voltage jumps. b) Similarly, the current-voltage characteristics for somewhat longer devices B_{5a} and B_{5b} ($L = 150$, and 170 nm), show similar voltage steps at low voltages.

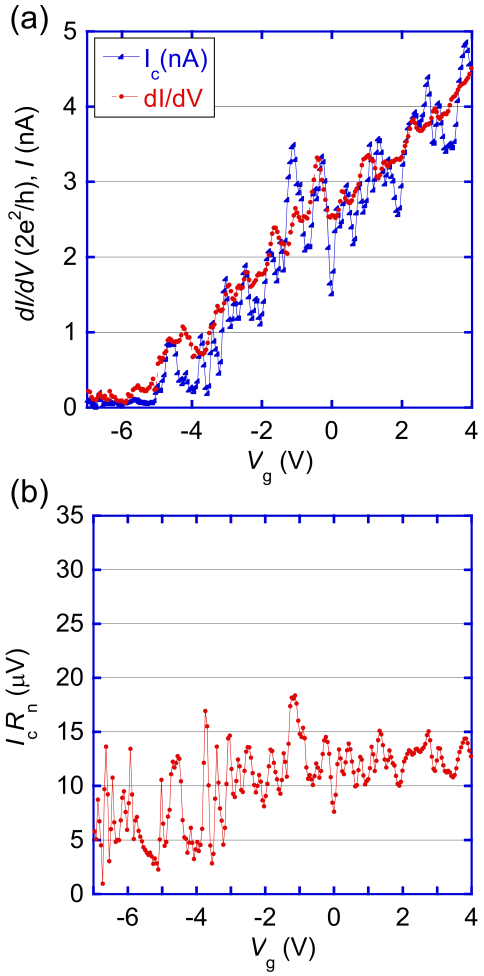

FIG. 14. (a) Normal state conductance and critical current as a function of a local-gate voltage for device C_{11}. After opening of the first conducting channel at $V_g \approx -5$V, the overall conductance and critical current increase linearly with the gate voltage. (b) I_cR_n product as a function of gate voltage. The constant value indicates that the critical current is correlated with the normal state conductance.

the nanowires, the conductance and the critical current are strongly suppressed at large negative gate voltages, $V_g < -5\,\mathrm{V}$. Changing the gate voltage towards positive values results in linear increase of the averaged conductance and critical current, the latter reaching the value of $I_c = 4\,\mathrm{nA}$ at $V_g = 3\,\mathrm{V}$. Simultaneously, the I_cR_n product saturates at the value, $I_cR_n = 12.5\,\mu\mathrm{V}$, and remains constant over a wide range of gate voltages, Fig. 14b.

In Fig. 15a we present a set of IVCs for the suspended device C_{12} ($L \approx 200\,\mathrm{nm}$ and $R_n = 3.6\,\mathrm{k\Omega}$) for gate voltages ranging from $V_g = -2.16$V to $V_g = +0.92$V. At large positive gate voltage, *i.e.* at large conductance, the IVC shows significant excess current and enhanced subgap conductance, indicating highly transmissive SNS regime (see Fig. 15). In the opposite limit of large negative gate voltage (small conductance), the IVC has a typical form for SIS tunnel junctions with negative excess current[38] and strongly suppressed subgap conductance (Fig. 15). The suppression of the subgap conductance is explained by small probability of MAR processes at small voltage, which scales with $\mathcal{D}^n$, where $n = 2\Delta/eV$ is the number of Andreev reflections. In the tunneling regime with small $\mathcal{D} \ll 1$ the subgap conductance is exponentially small. At the intermediate gate voltages the device exhibits continuous crossover between these two regimes in accordance with the theoretical predictions for contacts with varying transparency.[29,42]

IX. CONCLUSION

We have investigated, both experimentally and theoretically, proximity effect in InAs nanowires connected to superconducting electrodes. We have fabricated and investigated a large number of nanowire devices with

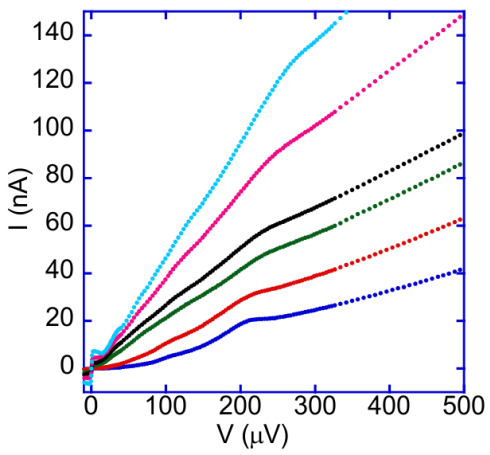

FIG. 15. Current-voltage characteristics for device C_{12} of length $L = 200\,\text{nm}$. for different gate voltages, $V_g = -2.16, -1.86, -1.64, -1.40, -0.93, 0.92\text{V}$ (from bottom to top). The IVC exhibit cross over from the tunneling regime with small subgap current and negative excess current to the SNS regime with enhanced subgap conductance and positive excess current.

suspended gate controlled nanowires and non-suspended nanowires, with a broad range of lengths and normal state resistances. We measured current-voltage characteristics and analyzed their main features: the Josephson current, excess current, and subgap current as functions of length, temperature, magnetic field and gate voltage, and compared them with theory. The devices show reproducible resistance per unit length, and highly transmissive interfaces. The measured superconducting characteristics are consistent and agree reasonably well in most cases with theoretically computed values. The Josephson critical current for a short length device, $L = 30\,\text{nm}$, exhibits a record high magnitude of 800 nA at low temperature that comes close to the theoretically expected value. The critical current in other devices is typically reduced compared to the theoretical values. The measured excess current in most of the devices is consistent with the normal resistance data and agrees well with the theory. The subgap current shows large number of structures, some of them are identified as subharmonic gap structures generated by MAR. The other structures, detected in both suspended and non-suspended devices, have the form of the voltage steps at voltages that are independent of either the superconducting gap or the length of the wire. By varying the gate voltage in suspended devices we were able to observe a cross over from typical tunneling transport, with suppressed subgap current and negative excess current, at large negative gate voltage to pronounced SNS-type behavior, with enhanced subgap conductance and large positive excess current, at large positive gate voltage.

ACKNOWLEDGMENTS

We acknowledge fruitful discussions with Lars Samuelson, Christopher Wilson and Jonas Bylander. The work was supported by the Swedish Research council, the Wallenberg foundation. HQX also acknowledges the National Basic Research Program of the Ministry of Science and Technology of China (Nos. 2012CB932703 and 2012CB932700).

* abay@chalmers.se
† per.delsing@chalmers.se

[1] L. Samuelson, Mater. Today **6**, 22 (2003).
[2] C. Thelander, P. Agarwal, S. Brongersma, J. Eymery, L. Feiner, A. Forchel, M. Scheffler, W. Riess, B. Ohlsson, U. Gsele, and L. Samuelson, Mater. Today **9**, 28 (2006).
[3] Y. Li, F. Qian, J. Xiang, and C. M. Lieber, Mater. Today **9**, 18 (2006).
[4] S. A. Dayeh, Semicond. Sci. and Technol. **25**, 024004 (2010).
[5] I. van Weperen, S. R. Plissard, E. P. A. M. Bakkers, S. M. Frolov, and L. P. Kouwenhoven, Nano Lett. **13**, 387 (2013).
[6] S. Abay, D. Persson, H. Nilsson, H. Q. Xu, M. Fogelström, V. Shumeiko, and P. Delsing, Nano Lett. **13**, 3614 (2013).
[7] T. S. Jespersen, M. L. Polianski, C. B. Sørensen, K. Flensberg, and J. Nygård, New J.Phys. **11**, 113025 (2009).
[8] J. Xiang, A. Vidan, M. Tinkham, R. M. Westervelt, and M. Lieber, Charles, Nat. Nanotechnol. **1**, 208 (2006).
[9] Y.-J. Doh, J. A. van Dam, A. L. Roest, E. P. A. M. Bakkers, L. P. Kouwenhoven, and S. De Franceschi, Science **309**, 272 (2005).
[10] H. A. Nilsson, P. Samuelsson, P. Caroff, and H. Q. Xu, Nano Lett. **12**, 228 (2012).
[11] S. Abay, H. Nilsson, F. Wu, H. Xu, C. Wilson, and P. Delsing, Nano Lett. **12**, 5622 (2012).
[12] T. Nishio, T. Kozakai, S. Amaha, M. Larsson, H. A. Nilsson, H. Q. Xu, G. Zhang, K. Tateno, H. Takayanagi, and K. Ishibashi, Nanotechnology **22**, 445701 (2011).
[13] Y.-J. Doh, S. D. Franceschi, E. P. A. M. Bakkers, and L. P. Kouwenhoven, Nano Lett. **8**, 4098 (2008).
[14] L. Hofstetter, S. Csonka, J. Nygård, and C. Schönenberger, Nature **461**, 960 (2009).
[15] V. Mourik, K. Zuo, S. M. Frolov, S. R. Plissard, E. P. A. M. Bakkers, and L. P. Kouwenhoven, Science **336**, 1003 (2012).
[16] M. T. Deng, C. L. Yu, G. Y. Huang, M. Larsson, P. Caroff, and H. Q. Xu, Nano Lett. **12**, 6414 (2012).
[17] A. Das, Y. Ronen, Y. Most, Y. Oreg, M. Heiblum, and H. Shtrikman, Nature Phys. **8**, 887 (2012).
[18] I. Kulik and A. Omel'yanchuk, Sov. Phys.–JETP Letters **21**, 96 (1975).
[19] A. Kretinin, A. Das, and H. Shtrikman, arXiv:1303.1410.
[20] J. Meyer and G. Minnigerode, Phys. Lett. A **38**, 529 (1972).
[21] W. Skocpol, M. Beasley, and M. Tinkham, J. Low Temp. Phys. **16**, 145 (1974).
[22] B. Ohlsson, Physica E **13**, 1126 (2002).

[23] H. A. Nilsson, T. Duty, S. Abay, C. Wilson, J. B. Wagner, C. Thelander, P. Delsing, and L. Samuelson, Nano Lett. **8**, 872 (2008).
[24] D. B. Suyatin, C. Thelander, M. T. Björk, I. Maximov, and L. Samuelson, Nanotechnology **18**, 105307 (2007).
[25] S. Datta, *Electronic Transport in Mesoscopic Systems* (Cambridge University Press, 1997).
[26] P. Samuelsson, A. Ingerman, G. Johansson, E. V. Bezuglyi, V. S. Shumeiko, G. Wendin, R. Kürsten, A. Richter, T. Matsuyama, and U. Merkt, Phys. Rev. B **70**, 212505 (2004).
[27] A. Furusaki, H. Takayanagi, and M. Tsukada, Phys. Rev. B **45**, 10563 (1992).
[28] G. Arnold, J. Low Temp. Phys. **68**, 1 (1987).
[29] E. N. Bratus', V. S. Shumeiko, and G. Wendin, Phys. Rev. Lett. **74**, 2110 (1995).
[30] D. Averin and A. Bardas, Phys. Rev. Lett. **75**, 1831 (1995).
[31] J. C. Cuevas, A. Martín-Rodero, and A. L. Yeyati, Phys. Rev. B **54**, 7366 (1996).
[32] Cross over from diffusive short- to long-junction regime could alternatively be modeled with a theory developed in Ref. 38.
[33] J. C. Cuevas and M. Fogelström, Phys. Rev. B **64**, 104502 (2001).
[34] M. Eschrig, Phys. Rev. B **80**, 134511 (2009).
[35] A. V. Zaitsev, Sov. Phys. –JETP **59**, 1015 (1984).
[36] V. S. Shumeiko, E. N. Bratus, and G. Wendin, Low Temp. Phys. **23**, 181 (1997).
[37] J. C. Cuevas, J. Hammer, J. Kopu, J. K. Viljas, and M. Eschrig, Phys. Rev. B **73**, 184505 (2006).
[38] E. V. Bezuglyi, E. N. Bratus', and V. S. Shumeiko, Phys. Rev. B **83**, 184517 (2011).
[39] M. Y. Kupriyanov, A. Brinkman, A. A. Golubov, M. Siegel, and H. Rogalla, Physica C **326**, 16 (1999).
[40] G. E. Blonder, M. Tinkham, and T. M. Klapwijk, Phys. Rev. B **25**, 4515 (1982).
[41] V. Galaiko and N. Kopnin, in *Nonequilibrium Superconductivity*, edited by D. Langenberg and A. Larkin (North-Holland, Amsterdam, 1986).
[42] A. Ingerman, G. Johansson, V. S. Shumeiko, and G. Wendin, Phys. Rev. B **64**, 144504 (2001).